Available online at www.sciencedirect.com
ScienceDirect
Trans. Nonferrous Met. Soc. China 34(2024) 3693−3706
Transactions of Nonferrous Metals Society of China
www.tnmsc.cn

Enhancing zinc storage performance of Mn_3O_4 cathode through Ag-doping and -crosslinking dual-modification strategy

Xin-yuan WANG[1], Tian-zhen JIAN[1], Ya-ting YANG[1], Jian-ping MA[2], Xian-hong LI[2], Zi-long XUE[1], Wen-qing MA[1,2,3], Cai-xia XU[1]

1. Institute for Advanced Interdisciplinary Research, Collaborative Innovation Center of Technology and Equipment for Biological Diagnosis and Therapy in Universities of Shandong, School of Chemistry and Chemical Engineering, University of Jinan, Jinan 250022, China;
2. Shandong Sacred Sun Power Sources Co., Ltd., Qufu 273100, China;
3. State Key Laboratory of Crystal Materials, Shandong University, Jinan 250100, China

Received 22 February 2023; accepted 7 November 2023

Abstract: Octahedral Mn_3O_4 nanoparticles with an Ag-doping and nanoporous Ag (NPS) framework was simply fabricated through an alloying-etching engineering. The dual-modified Mn_3O_4 (denoted as Ag−Mn_3O_4/NPS) consists of Ag-doped Mn_3O_4 nanoparticles crosslinked with three dimensional nanoporous Ag framework. The incorporated Ag dopant is effective in improving the intrinsic ionic and electronic conductivities of Mn_3O_4, while the NPS framework is introduced to improve the electron/mass transfer across the entire electrode. Profiting from the dual-modification strategy, the Ag−Mn_3O_4/NPS exhibits admirable rate capability and cycling stability. A high reversible capacity of 88.7 mA·h/g can still be retained for over 1000 cycles at a current density of 1 A/g. Moreover, a series of ex-situ experimental techniques indicate that for Ag−Mn_3O_4/NPS electrode during the zinc ion storage, Mn_3O_4 is electrochemically oxidized into various MnO_x (e.g., Mn_2O_3, MnO_2) species in the initial charging, and the subsequent battery reaction is actually the intercalation/deintercalation of H^+ and Zn^{2+} into MnO_x.
Key words: Ag-doped Mn_3O_4; zinc ion battery; nanoporous Ag; dealloying

1 Introduction

In recent years, large-scale energy storage technologies have garnered ever-increasing attention because they can integrate the renewable but spatially and temporally inhomogeneous energy sources (e.g., wind and solar) into the grid [1−3]. Among various energy storage devices, aqueous zinc ion batteries (AZIBs) using metallic Zn as anode and water as electrolyte solvent are considered as the promising one due to their competitive advantages in security, cost-effectiveness, and environmental benignity [4−6]. In particular, the ionic conductivity of aqueous electrolytes (~1 S/cm) is higher than that of the nonaqueous ones (~10^{-3}–10^{-2} S/cm), which is well fitted for the high-power input/output requirement of battery-energy power station [7−10]. Despite the uplifting prospect, the application of AZIBs is still depressed by the unestablished and complicated battery reactions and the unsatisfied battery performances [2,4,11]. To overcome this limitation, tremendous research effort has been launched for the screening of high-performance cathode materials, such as hexacyanoferrates, polyanionic compounds, and

Corresponding author: Wen-qing MA, Tel: +86-531-82767046, E-mail: ifc_mawq@ujn.edu.cn;
Cai-xia XU, Tel: +86-531-82767046, E-mail: chm_xucx@ujn.edu.cn
DOI: 10.1016/S1003-6326(24)66634-3

vanadium- and manganese-based oxides/ sulfides. As so far, inspiring breakthrough has been made to further enhance the performances of AZIBs [2]. Among them, manganese oxides (MnO_x) are considered as the promising candidates due to their innate advantages of natural abundance, low-cost, and eco-friendliness [12−19]. However, the application prospect of MnO_x is gloomy due to their inherently poor ionic and electronic conductivities [20−24].

Currently, lattice doping that can trigger strong ionic bonding (electronic interaction) between metal ions and lattice oxygen was proposed and proven to be effective in improving ion and electron transportation of metal oxides [25−32]. The ion-doped metal oxides usually show novel crystal structure with distinguished physicochemical and electrochemical properties as compared to their undoped counterparts [30−33]. For instance, DAI et al [30] reported that the electronic distribution, morphology, and the conductivity of α-MnO_2 can be modified by Ag-doping. Recently, many researches [29,33] found that the ion dopant (e.g., Ni^{2+} and Cu^{2+}) can effectively improve the inherent stability with inhibited structure collapse, the Mn-dissolution, and the Zn storage reaction kinetics of MnO_x.

Similar to other electrochemical energy storage systems like lithium ion batteries [31], the microstructure of electrode materials is considered as another key factor for improving battery reaction kinetics [34,35]. For the MnO_x cathode structure, it is preferable with large surface area for achieving more active sites, abundant pores for facilitating mass transfer, and high electronic conductivity for improving electron transportation of MnO_x [2,25]. With this recognition, nanoporous spongy materials, which possess three-dimensional (3D) bicontinuous porous structure, have been accepted as the ideal choice to meet the needs of cathode material due to their interconnected channels/ligaments for mass transfer and large surface area for active site exposure [35−37].

Dealloying is a simple yet highly effective method for the straightforward fabrication of spongy metal, oxide, and their complexes. For the dealloying of various transition metal–Al (e.g., Mn, Fe, Co, and Ti, etc.) binary alloys, the highly reactive Al atoms can be readily etched out, while the transition metal atoms are simultaneously oxidized by OH^- and dissolved oxygen [38,39]. Whereas, the chemically inert metals (e.g., Cu, Ag, Pd, Pt, and Au, etc.) will self-reassemble into a spongy structure by surface diffusion and aggregation at the metal−electrolyte interface when dealloying their Al-based precursors [38−40]. Even so, a tiny amount of oxidation of these chemically inert metals is usually observed since their newly exposed atoms have ultrahigh surface energy and thus would be partially oxidized during the dealloying process. Given that, chemically inert metals can act as an ideal foreign component for achieving the as-proposed dual-modification strategy.

In current work, we commit to promote the zinc storage performance of Mn_3O_4 through an Ag-doping and nanoporous Ag (NPS)-crosslinking dual-modification strategy (denoted as Ag−Mn_3O_4/NPS). Ag is selected to function as a proof-of-concept owing to its comprehensive advantages in cost, chemical reactivity, and conductivity. The Ag−Mn_3O_4/NPS and Mn_3O_4 (the control sample) were prepared through alloying-etching engineering by immersing the precursor alloys of $Ag_1Mn_9Al_{90}$ and $Mn_{10}Al_{90}$ into NaOH solution, respectively. Benefiting from the dual-modification strategy, the Ag−Mn_3O_4/NPS shows much better electrochemical performances than Mn_3O_4. Moreover, the zinc ion storage mechanism was elucidated by using ex-situ XRD, Raman, and XPS, which indicates that the Ag−Mn_3O_4 is electrochemically oxidized into various Ag−MnO_x (e.g., Mn_2O_3 and MnO_2) during initial charging. The subsequent battery reaction is actually the intercalation/deintercalation of H^+ and Zn^{2+} into MnO_x. This work can promote the understanding of the Zn ion storage mechanism of low-valence (valence value <4) MnO_x, while the Ag-doping and nanoporous Ag-crosslinking dual-modification strategy provides a promising avenue to design high-performance cathode for zinc ion batteries.

2 Experimental

2.1 Material preparation

The $Ag_1Mn_9Al_{90}$ and $Mn_{10}Al_{90}$ (at.%) precursors were prepared by melting the corresponding pure (>99.99 wt.%) metals in an arc furnace under the atmosphere of Argon (Ar) and

spinning in a high vacuum rotary quenching system. The as-prepared alloy ribbons were then immersed into 1 mol/L NaOH aqueous solution for selectively dissolving of Al. Afterwards, the as-obtained samples were collected by washing with deionized (DI) water, drying under vacuum, and storing in a cool dry place in air condition.

2.2 Material characterization

The X-ray diffraction (XRD) was performed on a Bruker D8-advance X-ray diffractometer with Cu K_α radiation (λ=1.5481 Å). The Raman spectra were recorded on a laser microscopic confocal Raman spectrometer (Horiba Scientific LabRAM HR Evolution) with an excitation wavelength of 532 nm. The surface elemental information was studied by using an X-ray photoelectron spectrometer (XPS, Thermo Fisher Scientific ESCALAB 250Xi) with Al K_α X-ray excitation source and C 1s (284.6 eV) as the reference line. The morphology of these samples was observed by using a scanning electron microscope (SEM, JEOL JSM−6700) and a transmission electron microscope (TEM, JEOL JEM−2100).

2.3 Electrochemical measurement

The electrochemical performances of the as-prepared samples were studied by using 2032 coin-type cells with Zn foil as anode. The working electrode was prepared by dispersing a mixture of active material (70 wt.%), conductive carbon (super P, 20 wt.%), and polyvinylidene fluoride (10 wt.%) into *N*-methyl pyrrolidinone to form a homogeneous electrode slurry. The slurry was then painted onto a titanium foil and fully dried at 60 °C. The mass loading of active substance on the electrode was 0.6−0.8 mg/cm^2. The electrolyte was a mixed aqueous solution of $ZnSO_4$ (2 mol/L) and $MnSO_4$ (0.1 mol/L). The galvanostatic discharge/charge (GDC) and cyclic voltammetry (CV) measurements were performed on a Neware battery test system and a CHI 760E electrochemical workstation, respectively. The electrochemical impedance spectroscopy (EIS) was performed in the frequency range of 10^5−10^{-2} Hz. For battery chemistry study, the cells were stopped at different state-of-charge (SOC) to retrieve their electrodes for ex-situ characterization. The as-retrieved electrodes were fully washed with DI water and dried in ambient condition before use.

3 Results and discussion

3.1 Structure analysis

As schematically shown in Fig. 1, the Ag−Mn_3O_4/NPS was prepared through alloying-etching engineering. A ternary alloy of $Ag_1Mn_9Al_{90}$ (by atom) was manufactured and used as the precursor. As shown in Fig. S1(a) of Supporting Information (SI), the $Ag_1Mn_9Al_{90}$ alloy is mainly composed of Al and various intermetallic compounds (e.g., $AlAg_3$, AlMn, $Al_{81}Mn_{19}$, Al_6Mn, and $Al_{0.27}Mn_{0.73}$, Ag_7Mn_3, etc.). Owing to the difference in chemical properties, the elements of Ag, Mn, and Al show distinctly different evolution behaviors in alkaline solution. Once immersing into the NaOH aqueous solution, Al would be selectively removed while the newly exposed Mn atoms were simultaneously oxidized by OH^- and dissolved oxygen species at the solid−liquid interface [38,39].

The phase composition of Ag−Mn_3O_4/NPS was identified by using XRD, Raman, and XPS. As shown in Fig. 2(a), the XRD pattern of Ag−Mn_3O_4/NPS depicts two sets of diffraction peaks, which can be indexed to Mn_3O_4 (JCPDS #24-0734) and metallic Ag (JCPDS #65-2871). Interestingly, the diffraction peaks of (112), (103), (211), (004), and (220) show slight negative-shift, indicating that

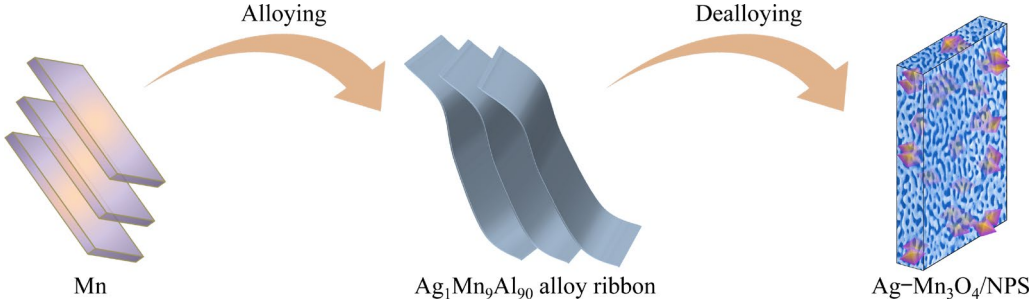

Fig. 1 Schematic diagram of preparation process of Ag−Mn_3O_4/NPS

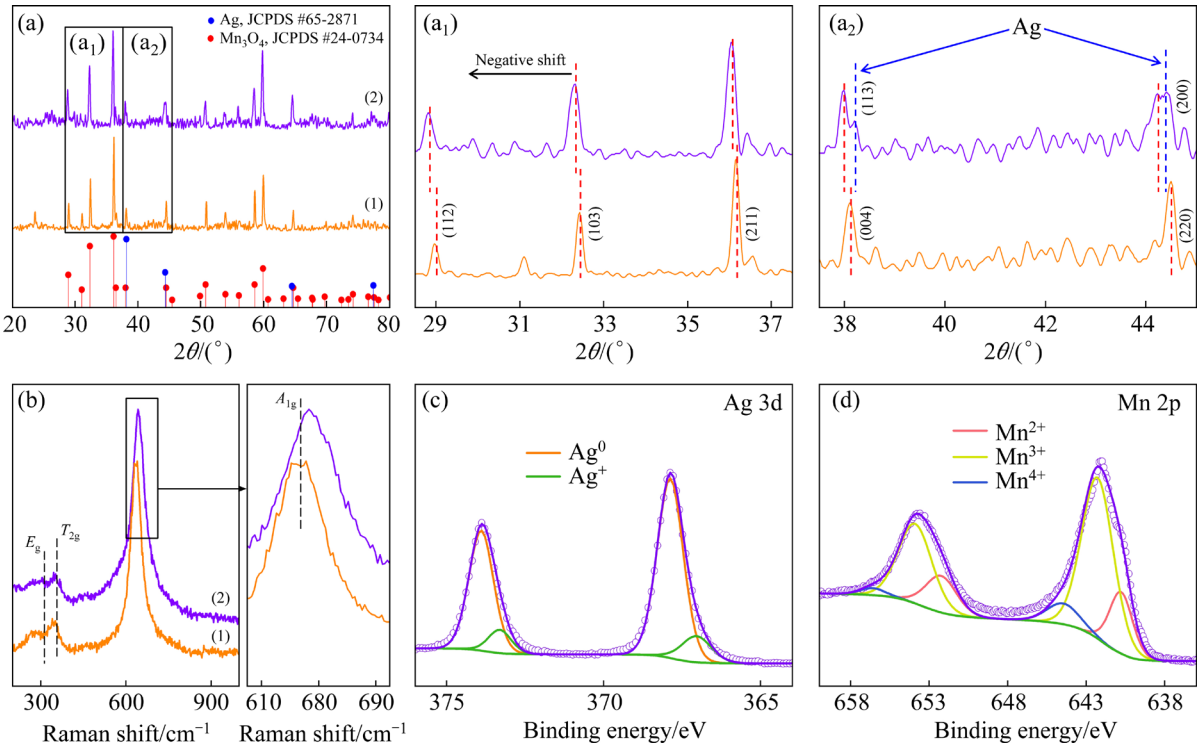

Fig. 2 XRD patterns (a, a_1, a_2) and Raman spectra (b) of Mn_3O_4 (1) and Ag−Mn_3O_4/NPS (2) samples, and XPS spectra of Ag−Mn_3O_4/NPS (c, d)

some of the Ag might be incorporated into the crystal structure of Mn_3O_4, and thus resulted in an increment of the interplanar spacing according to the Bragg's law (Figs. 2(a_1, a_2)) [29,30,32]. Based on these analyses, the sample derived from $Ag_1Mn_9Al_{90}$ is mainly composed of Ag and Ag-doped Mn_3O_4. It should be noted that several weak peaks can also be observed at 2θ range of 25°−30° on Ag−Mn_3O_4/NPS, which can be well indexed to the Ag_3Al (JCPDS #28-0034). This is attributed to the anticorrosion difference among different phases (Al and various intermetallic compounds) in the precursor $Ag_1Mn_9Al_{90}$ alloy.

For comparison, a binary alloy of $Mn_{10}Al_{90}$ was prepared and subjected to dealloying process. The diffraction peaks of the as-obtained dealloying product matched well with the standard PDF card of Mn_3O_4. Moreover, as depicted in Fig. 2(a_1), the width of diffraction peaks of the Ag-doped Mn_3O_4 is broadened as compared to Mn_3O_4, illustrating the decrement of the grain size. Moreover, a small peak at 23° is also observed corresponding to Mn_2O_3 (JCPDS #33-0900), indicating that some of the Mn atoms have been over-oxidized in the dealloying process. Interestingly, Mn_2O_3 related sign cannot be observed on Ag−Mn_3O_4/NPS. This phenomenon originated from two main reasons. First, the Ag−Mn intermetallic compounds in $Ag_1Mn_9Al_{90}$ have relatively high anticorrosion and antioxidation abilities, thereby delaying the oxidation of Mn [40,41]. Second, the incorporation of Ag can change the chemical microenvironment (e.g., atom coordination, electron configuration, and bond-type) of Mn_3O_4, and also improve its antioxidation ability. Note that, the amount of Mn_2O_3 is less in the dealloying product of $Mn_{10}Al_{90}$, therefore the resultant sample is denoted as Mn_3O_4 for simplicity.

The phase composition and evolution of the two samples were further characterized by Raman technique. As shown in Fig. 2(b), the out-of-plane bending of MnO_x (E_g mode), an asymmetric stretch of Mn−O−Mn (T_{2g} mode), and the stretching vibration of Mn−O (A_{1g} mode) are clearly recorded on both Ag−Mn_3O_4/NPS and Mn_3O_4 [29,42]. The Mn—O bond in Ag−Mn_3O_4/NPS has obvious shift, which should be ascribed to the introduction of lattice Ag (Fig. 2(b)) [30]. Moreover, the intensity between the peaks at ~643 and ~345 cm^{-1} is increased, implying that the electronic structure is changed upon the incorporation of Ag [29,30].

XPS analysis was further performed to

understand the chemical bonding information of Ag−Mn_3O_4/NPS. As shown in Fig. 2(c), the Ag 3d spectrum depicts two pairs of sub-peaks located around 373.9/367.9 and 373.3/367.1 eV, which are assigned to Ag^0 and Ag^+, respectively [30]. These results indicate that most of Ag atoms have remained in metallic state, while a small portion of Ag atoms are successfully incorporated into the crystal structure of Mn_3O_4. Moreover, the Mn 2p spectrum of Ag−Mn_3O_4/NPS can be deconvoluted into three couplets of sub-peaks located at 652.2/640.8, 653.9/642.3, and 656.6/644.5 eV, which are associated with Mn^{2+}, Mn^{3+} and Mn^{4+} species, respectively (Fig. 2(d)) [12, 43]. The Mn^{4+} should stem from the surface oxidation of the sample during the dealloying and/or drying process [40,44]. The compositions of Ag−Mn_3O_4/NPS were quantitatively estimated using energy dispersive spectroscopy (EDS) analysis. The atomic ratios of Ag and Mn after etching are 4.92% and 43.35%, respectively (Fig. S1(b) in SI). The integral area ratio of Ag^+-to-Ag^0 in the pristine electrode is calculated to be ~20.4%, indicating that the ratio of Ag dopant is ~0.83% in Ag−Mn_3O_4/NPS.

The morphological information of the Mn_3O_4 and Ag−Mn_3O_4/NPS was collected by SEM and TEM. As shown in Figs. 3(a), (b), and (S2), both the Ag-doped Mn_3O_4 and Mn_3O_4 octahedra have the particle size around 200 nm. The Ag-doped Mn_3O_4 sample shows one interesting dual structure characterized by the nanoparticles crosslinked with spongy framework. As shown in Figs. 3(e−h), the Mn, O and Ag are matched well with the outline of the sample, and the signal of Ag is strengthened whereby the spongy materials gathered. Consequently, the sample derived from $Ag_1Mn_9Al_{90}$ is indeed an integral nanohybrid of Ag-doped Mn_3O_4 and NPS as schematically shown in Fig. 1. The crosslinked morphology is also proven by TEM (Fig. 3(c)). The HRTEM image inset in Fig. 3(c) clearly depicts the lattice fringes with a *d*-space of 2.56 Å, which is ~0.07 Å larger than the corresponding interplanar spacing of (211) of Mn_3O_4. This observation is well consistent with the negative shift of the (211) diffraction peak of Ag−Mn_3O_4 in Fig. 2(a_1), and further confirmed the successful Ag-incorporation in Mn_3O_4 crystal structure. Moreover, the selected area electron diffraction (SAED) pattern reflects the poly-crystalline characteristic of Ag−Mn_3O_4/NPS (Fig. 3(d)). The specific architecture of Ag−Mn_3O_4/NPS offers interconnected metallic skeleton for electron transportation, abundant channels for electrolyte penetration, and sufficient active site for Zn^{2+} intercalation/deintercalation.

3.2 Zinc ion storage performance

The zinc ion storage mechanism and performance of Ag−Mn_3O_4/NPS were comprehensively studied by using various spectroscopic, electron microscopic, and electrochemical techniques. Figure 4(a) shows the GDC profiles of Ag−Mn_3O_4/NPS performed in the voltage range of 0.7−1.8 V. In the first cycle, the

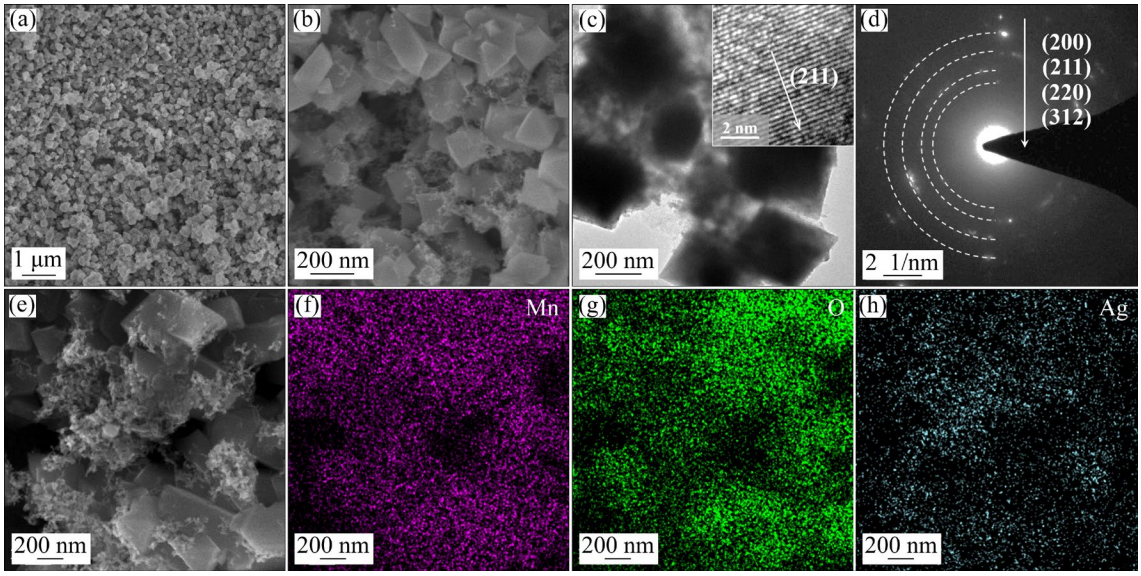

Fig. 3 SEM images (a, b), TEM and HRTEM (inset) image (c), SAED pattern (d), and EDS elemental mapping results (e−h) of Ag−Mn_3O_4/NPS

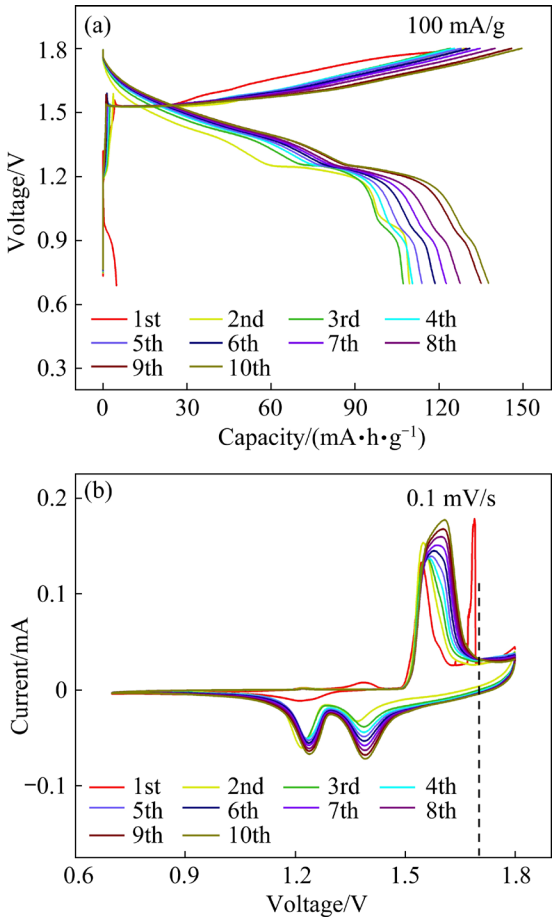

Fig. 4 GDC (a) and CV (b) curves of Ag−Mn_3O_4/NPS

Ag−Mn_3O_4/NPS shows an open circuit voltage of ~1.3 V and a discharge capacity of only 4.8 mA·h/g. However, the subsequent charging process delivers an abnormally high capacity of 129.8 mA·h/g. The initial GDC and its corresponding dQ/dV curves are distinctively different from the subsequent cycles. As shown in Fig. S3(b) of SI, the initial dQ/dV curve depicts a sharp oxidation peak centered at ~1.77 V. These results indicate that some energy-conversion-unrelated electrochemical oxidation reactions happened in the initial charge process. Moreover, the irreversible oxidation process in the initial cycle is also detected on the initial CV curve (Fig. 4(b); centered at ~1.69 V), which is well consistent with the GDC profile. These results imply that some of the battery components have been electrochemically oxidized in the initial charging process. Note that, the GDC profiles and the corresponding dQ/dV curves respectively show a small discharge plateau and a reduction peak at around 0.95 V, which can be ascribed to the formation of $(Zn(OH)_2)_3ZnSO_4·5H_2O$ (ZHS) due to the pH change originating from the gradual consumption of H^+ (see more details in Fig. S3 of SI).

To clarify this, the structure evolutions of the Ag−Mn_3O_4/NPS electrode at different SOCs were investigated by using ex-situ XRD, Raman, and XPS. As shown in Figs. 5(a−c), when discharged to 0.7 V, the newly emerged diffraction peaks at 29.3°, 31.2°, 33.0°, and 38.9° could be well assigned to $ZnMn_2O_4$ (JCPDS #24-1133). And the characteristic signals of MnOOH are also detected, which should originate from the insertion of H^+ [13,19,23]. It should be noted that, the strong diffraction peaks of (112), (200), (103), (211), (202), and (004) obviously shift to the much lower values, which should come from the intercalation of H^+ and/or Zn^{2+} [15,16]. Moreover, with the consumption of H^+, the left OH^- would combine with other species in the electrolyte (e.g., Zn^{2+}, SO_4^{2+}, and H_2O) at the electrolyte−electrode interface to form ZHS [12,16,43]. The ZHS related signal is also recorded on the high-resolution Zn 2p, Zn 3p, S 2P, and O 1s XPS spectra (Fig. 6). The content of both Mn^{2+} and Mn^{3+} slightly increased, which indicates that some of the Mn^{4+} has been reduced in the initial discharge process (Figs. 6(a) and S3). Moreover, the insertion of H^+/Zn^{2+} is also confirmed by the Ag 3d (the slight negative-shift of Ag^+ signal), O 1s (the increment of the peak intensity ratio between Mn—O—H and Mn—O—Mn), as well as the Zn 2p and Zn 3p (the appearance of the signals of intercalated Zn) spectra (Figs. 6(b–d) and (f)). Upon charging, the content of Mn^{4+} significantly increased while the values for Mn^{2+} and Mn^{3+} both show an obvious decrement (Figs. 6(a) and S4(a)). Meanwhile, the XRD pattern of the first charged electrode clearly depicts the diffraction peaks of MnO_2 (Figs. 5(b, c)). Moreover, the content of lattice Ag^+ in the discharged/charged electrodes is almost the same to that of the pristine one, which demonstrates that the Ag^+ does not participate in the ion extraction and intercalation reactions (Fig. S4(b)).

The evolutionary process is monitored by identifying the phase composition of the electrodes retrieved at different SOCs in the initial charging process. The electrode retrieved at 1.3 V shows the characteristic diffraction peaks of Mn_2O_3, whose signal faded with the raising charging potential. During the charging process, the strong diffraction peaks of (112), (200), (103), (211), (202), and (004)

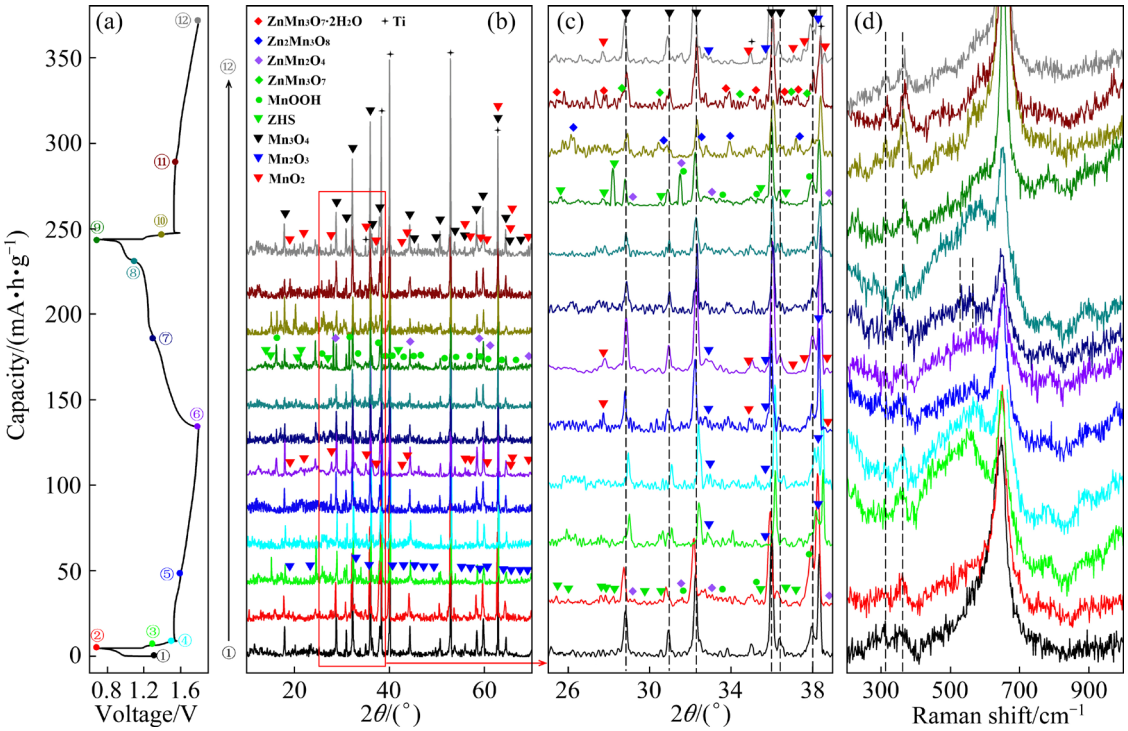

Fig. 5 GDC profiles (a), ex-situ XRD patterns (b, c), and Raman characterization (d) of Ag−Mn_3O_4/NPS electrode

gradually shift to higher values, implying the extraction of H^+/Zn^{2+} ions [15]. The oxidation process is also studied by using Raman (Fig. 5(d)). A broad peak ranging from 400 to 600 cm^{-1} is observed at the beginning of the charging process and its intensity decreases with the increase in charging potential.

By further driving the oxidation process to 1.8 V, MnO_2 related Raman signal is also recorded at 521.6 and 565.2 cm^{-1} [19,44]. This observation is coincident with XRD, XPS, and GDC results, which further confirmed the electrochemical oxidation of Mn_3O_4 to high-valence manganese oxides (Mn_2O_3 and MnO_2) in the initial recharging process. In the subsequent discharging, the discharge products can be indexed to Zn—Mn—O compounds with different stoichiometries (e.g., $Zn_2Mn_3O_8$, $ZnMn_3O_7$, $ZnMn_3O_7·2H_2O$, and $ZnMn_2O_4$, etc.) and MnOOH, which should be attributed to the insertion of Zn^{2+} and H^+, respectively. As expected, the Zn—Mn—O compounds and MnOOH gradually release ions and finally convert back manganese oxides during the second charging.

3.3 Zinc ion storage mechanism

To understand the effect of the introduced Ag, the zinc storage performances of Ag−Mn_3O_4/NPS and Mn_3O_4 were comparatively studied by using 2032 coin-type half-cells. Prior to the electrochemical measurements, the batteries were cycled by 10 times at 100 mA/g for battery formation and activation, which is not counted in the battery cycling number.

As shown in Fig. 7(a), the Ag−Mn_3O_4/NPS exhibits admirable rate capability, with discharge capacities of 102.5, 93.3, 86.3, and 80.9 mA·h/g at the current densities of 0.4, 0.6, 0.8, and 1.0 A/g, respectively. The discharge capacity retentions are about 91.0% (0.6 A/g), 84.2% (0.8 A/g), and 78.9% (1.0 A/g) of that at 0.4 A/g. Moreover, when the current densities switched back to 0.4 A/g, the capacities of Ag-Mn_3O_4/NPS relapsed much higher (Fig. 7(b)). For comparison, Mn_3O_4 was also tested under the same condition, which shows relatively lower discharge capacities at different current densities. As shown in Fig. S5(a) in SI, when the current densities changed back to 0.4 A/g, the 65th GDC profiles show an obvious gap with the 5th ones. In a word, the Ag-doping and NPS crosslinking dual-modification strategy effectively improved the rate performance of Mn_3O_4.

After the rate testing, both the Ag−Mn_3O_4/NPS and Mn_3O_4 were further tested at 1.0 A/g for cyclability evaluation by utilizing the 71st cycle as

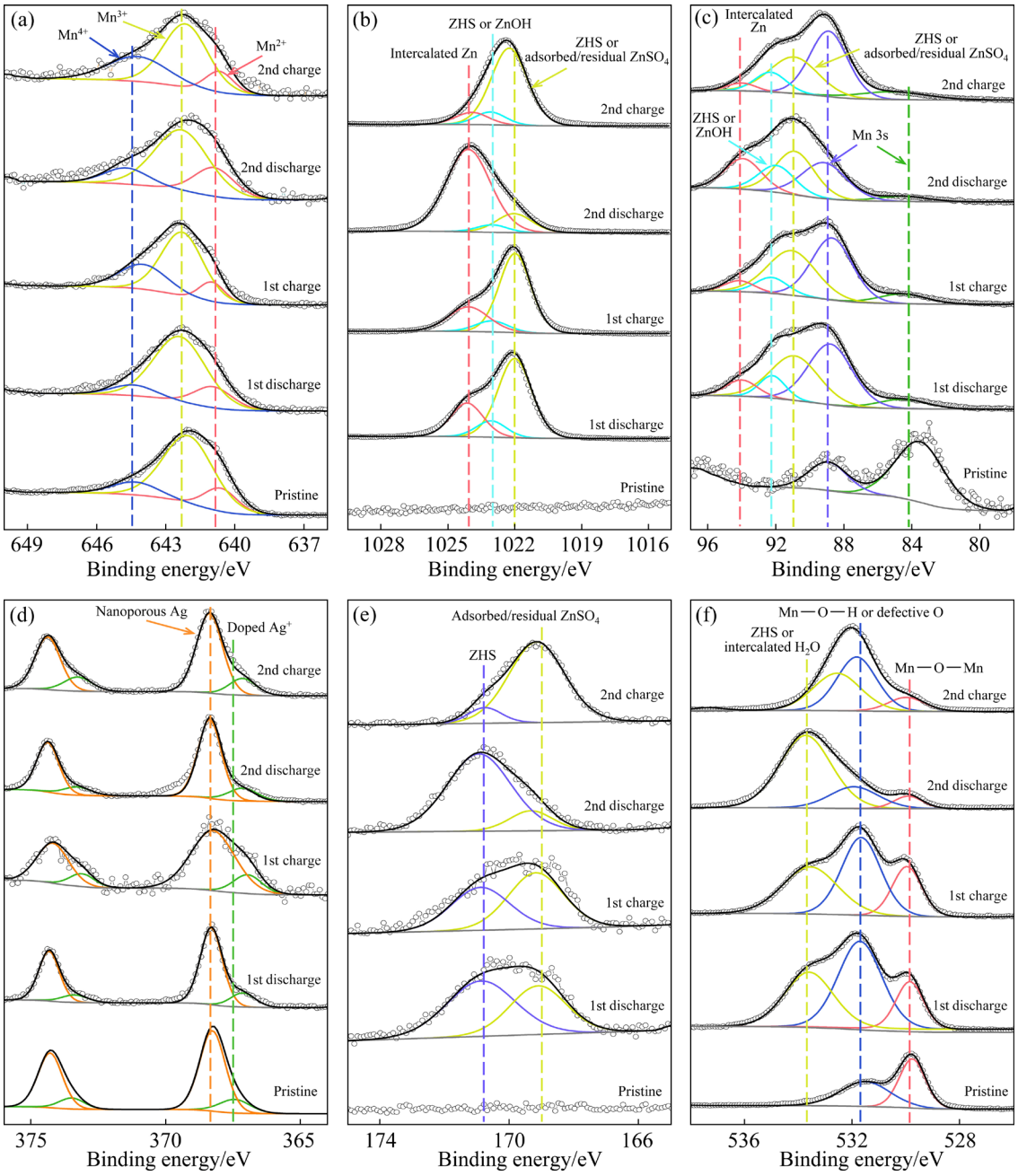

Fig. 6 Mn 2p (a), Zn 2p (b), Mn 3s, Zn 3p (c), Ag 3d (d), S 2p (e), and O 1s (f) XPS spectra of Ag−Mn_3O_4/NPS

the benchmark. As shown in Figs. 7 and S5, the capacity difference between Ag−Mn_3O_4/NPS and Mn_3O_4 grows gradually with the increase of cycling number. The capacity fading for Ag−Mn_3O_4/NPS is ~0.0036% per cycle after 70 cycles, which is much better than that of Mn_3O_4 (~0.028%). Moreover, the Ag−Mn_3O_4/NPS shows smaller polarization than that of Mn_3O_4 (Figs. 7(d), S5(c), and S5(d)). These results indicate that Ag that acts as both dopant and crosslinking network is effective in promoting the cycling and rate capability.

The battery reaction kinetics were systematically investigated by using various electrochemical techniques. Figure 8(a) shows the CV curves of Ag−Mn_3O_4/NPS obtained at different scan rates. With the increment in the scan rate, the cathodic and anodic peaks are both widened, and shift toward low and high values, respectively. Figure 8(b) shows the fitted curves regarding the linear relationship between the oxidation and reduction peak current (I_p) and the square root of the scanning rate ($v^{1/2}$). All of the peaks show a decent linear

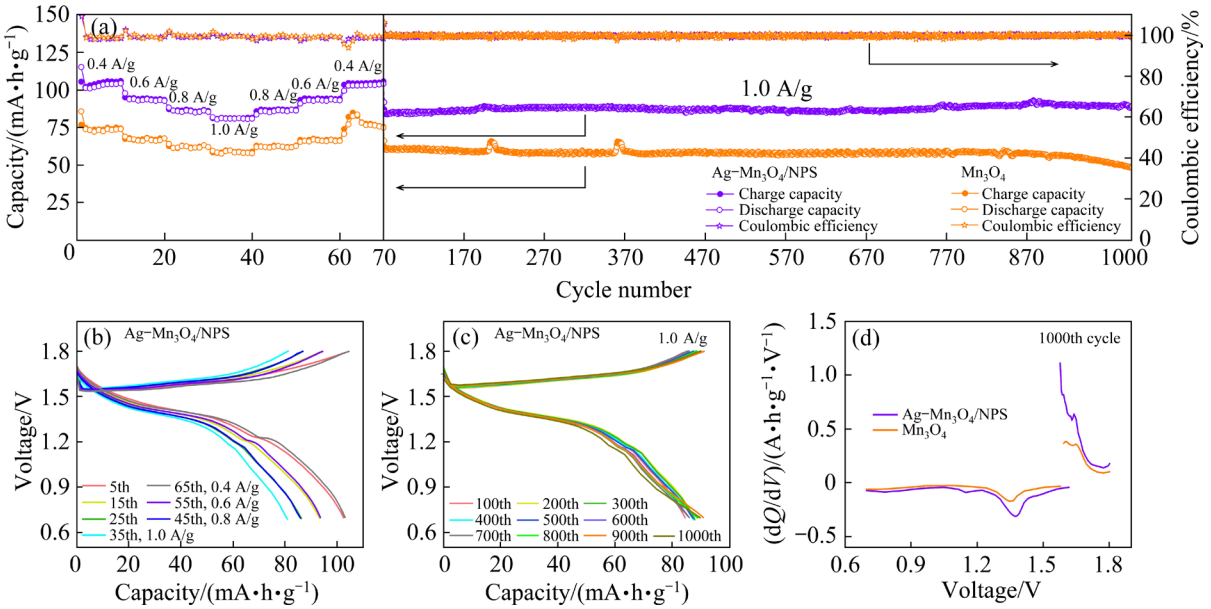

Fig. 7 Rate capability and subsequent long-term cycling stability of Ag−Mn_3O_4/NPS and Mn_3O_4 (a), and GDC profiles (b, c) and dQ/dV curves (d) of Ag−Mn_3O_4/NPS and Mn_3O_4

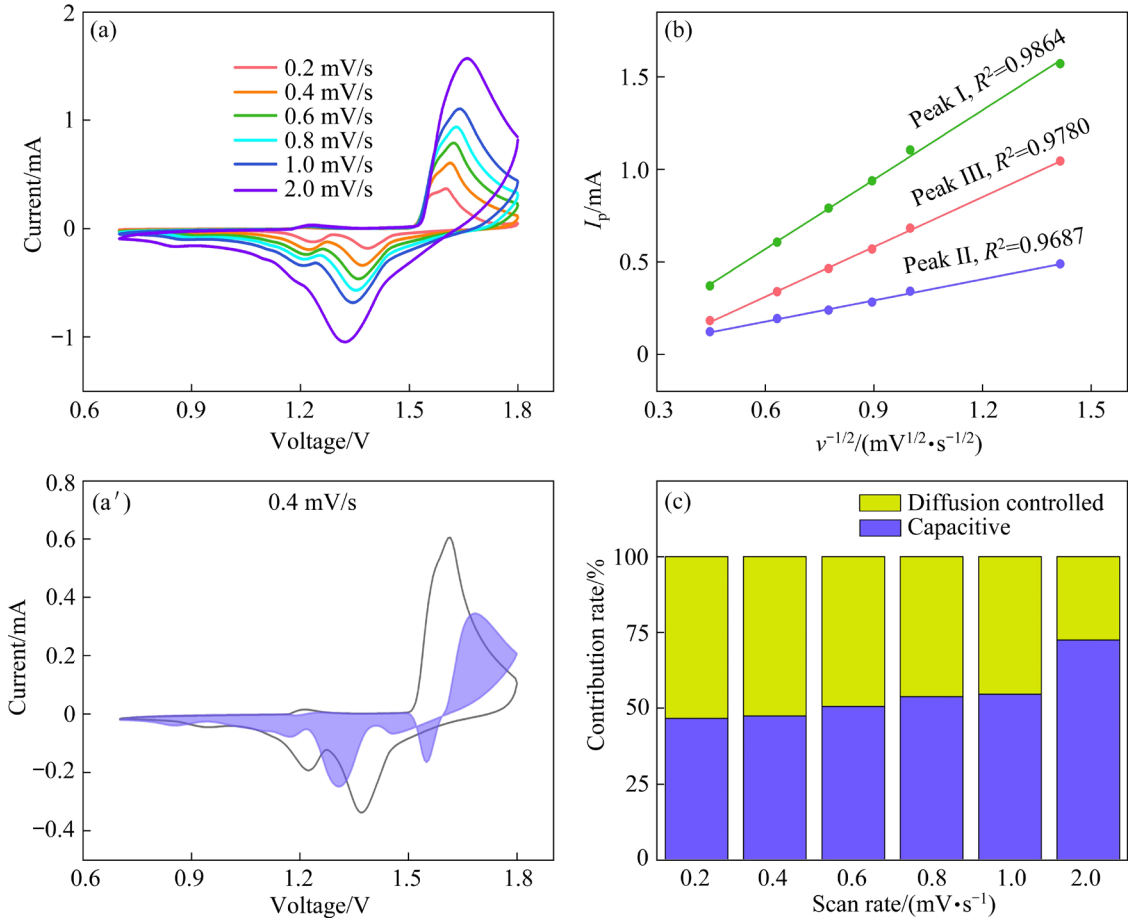

Fig. 8 CV curves (a, a′), simulation results of I_p−$v^{1/2}$ (b), and capacitive contribution rate (c) of Ag−Mn_3O_4/NPS

relationship between I_p and $v^{1/2}$ (R^2 for peak I, II, and III is 0.9864, 0.9687 and 0.9780, respectively), implying that the battery reaction is associated with ion diffusion.

$$I_p=0.4463nFAC\left(\frac{nFvD}{RT}\right)^{1/2} \quad (1)$$

$$I=k_1v+k_2v^{1/2} \quad (2)$$

$$D_{Li}=\frac{4}{\pi\tau}\left(\frac{m_BV_m}{M_BA}\right)^2\left(\frac{\Delta E_s}{\Delta E_\tau}\right)^2\left(\tau\ll L^2/D_{Ion}\right) \quad (3)$$

The apparent ion diffusion coefficient (D_{Ion}) can be estimated by using the Randles–Sevcik equation (Eq. (1)) [16,29,45]. Here, n is the number of the electron transferred in a certain electrochemical reaction process; F is the Faraday constant (96500 C/mol); A is the geometric area of the working electrode (cm^2); C is the ion concentration of Zn^{2+} (2 mol/L); v is the scanning rate (V/s); R is the molar gas constant (8.314 J/(mol·K)); T is the testing temperature (298.15 K). The apparent D_{Ion} of Ag−Mn_3O_4/NPS is ~5.89×10^{-13} cm^2/s. Moreover, the ion diffusion contribution rate was evaluated based on Eq. (2) [29,46], in which, k_1v and $k_2v^{1/2}$ are the parts of pseudo-capacitive and ion-diffusion contribution, respectively. For instance, 66.42% of the capacity of Ag−Mn_3O_4/NPS is associated with the ion diffusion at 0.4 mV/s (Figs. 8(a′, c)). The ion diffusion contribution rate at different scanning rates are calculated and intuitively summarized in Fig. 8(c) and S6 of SI. Obviously, the ion diffusion part contributes most of the capacity of Ag−Mn_3O_4/NPS at lower current densities but its contribution rate decreased when the scanning rate is raised.

The battery reaction kinetics of Ag−Mn_3O_4/NPS were further evaluated by using galvanostatic intermittent titration technique (GITT). As shown in Figs. 9, S7 and S8 of SI, the GITT was performed by pulse charging/discharging with a constant current of 50 mA/g for 10 min (τ) followed by standing for 60 min to reach steady state voltage (E_s). The D_{Ion} evolution was further analyzed as illustrated in Eq. (3) [16,46]. Here, V_m, M_B and m_B respectively represent the molar volume (cm^3/mol), molecular mass (g/mol) and mass (g) of the active material. A and L are the geometric area (cm^2) and thickness (cm) of the electrode, respectively. ΔE_τ is the voltage difference between the beginning and the end of the 10 min pulse process, while ΔE_s is

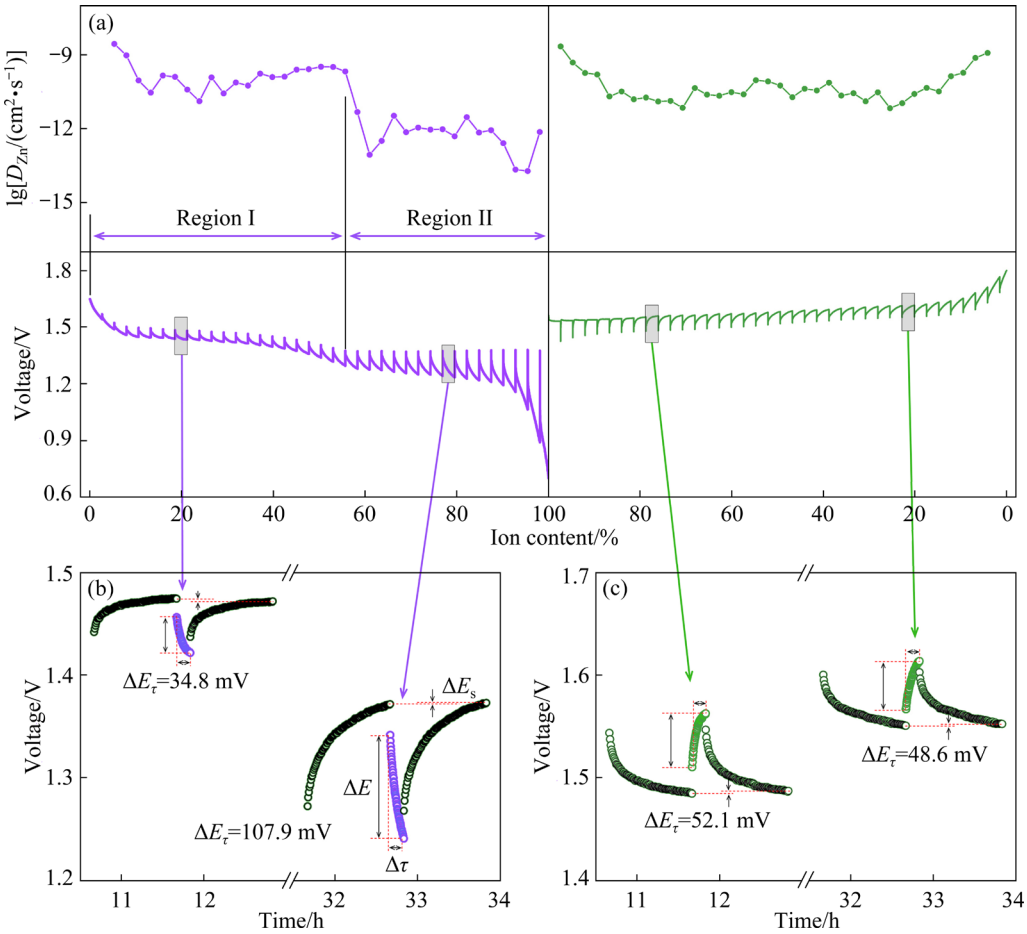

Fig. 9 GITT curve and corresponding ion diffusion evolution of Ag−Mn_3O_4/NPS (a), and titration processes selected from discharging (b) and charging (c), respectively

the E_s difference before and after an electrochemical process that contains a 10 min pulse and a 60 min standing process. The ohmic and charge transfer resistances are the main reasons accounting for the distinct voltage decrease at the beginning of discharging, while the subsequent voltage evolution is mainly associated with ion diffusion [16].

Figures 9(b) and S7 depict the evolutions of ΔE_τ, ΔE_s, and $(\Delta E_s/\Delta E_\tau)^2$. During discharging, the ΔE_τ in Region II is much larger, while the ΔE_s in Region II is obviously smaller than that in Region I. As a result, the $(\Delta E_s/\Delta E_\tau)^2$ in Region II is markedly smaller than that in the Region I, and so it is for D_{Ion}. As shown in Fig. 9(a), the D_{Ion} in Region I locates in the range of 4.72×10^{-12}–2.76×10^{-9} cm^2/s, which is several orders of magnitude higher than that in Region II (1.90×10^{-14}–3.33×10^{-12} cm^2/s). This result agrees well with the CV-derived apparent D_{Ion} (5.89×10^{-13} cm^2/s). In view of the remarkable difference in ion radius, Regions I and II are mainly dominated by H^+ and Zn^{2+} insertion, respectively. Subsequently, the D_{Ion} does not show sharp increment/decrement across the whole charging process (Figs. 9(a, c), S7 and S8), implying that the battery charging might be a H^+/Zn^{2+} synchronous extraction process.

Mn_3O_4 was also subjected to GITT test under the same condition (Fig. S9). The charge/discharge capacity of Mn_3O_4 is significantly lower than that of Ag−Mn_3O_4/NPS, which is coincident with the GDC result shown in Figs. 7 and S4. A distinct charge/discharge capacity difference is also recorded, which indicates that some irreversible reactions happened in the charging process (Figs. S8 and S10 of SI). Moreover, the D_{Ion} of Ag−Mn_3O_4/NPS is obviously higher than that of Mn_3O_4, which highlights the effectiveness of the dual-modification strategy in promoting the battery reaction kinetics. The EIS data further reveal that the Ag-doping and NPS-crosslinking dual-modification strategy works effectively in facilitating charge transfer kinetics in electrode (Fig. S11 of SI). Based on these results and analyses, the introduction of Ag, which serves as both dopant and conductive networks for Mn_3O_4, is beneficial for boosting the ion and electron transportation and thus greatly improves the electrochemical performance of Ag−Mn_3O_4/NPS toward zinc storage.

4 Conclusions

(1) An Ag-doping and nanoporous Ag (NPS)-crosslinking dual-modification strategy (Ag-Mn_3O_4/NPS) is proposed for improving the zinc storage performances of Mn_3O_4.

(2) The lattice Ag plays robust role in boosting the intrinsic ionic and electronic conductivities of Mn_3O_4, while the NPS framework greatly promotes the mass/electron transfer throughout the whole electrode.

(3) Benefiting from the dual-modification strategy, Ag−Mn_3O_4/NPS shows improved electrochemical performances (e.g., cycling stability, rate capability) as compared with Mn_3O_4.

(4) It is clearly demonstrated that the Ag−Mn_3O_4 gradually transformed (oxidized) into Ag−MnO_x in the first charging process, and the subsequent battery reaction is actually the H^+ and Zn^{2+} insertion/extraction into Ag−MnO_x.

CRediT authorship contribution statement

Xin-yuan WANG: Experiment operation, Data analysis, Literature research, Writing − Original draft; **Tian-zhen JIAN:** Data analysis, Literature research; **Ya-ting YANG:** Discussion, Formal analysis; **Jian-ping MA** and **Xian-hong LI:** Data analysis; **Zi-long XUE:** Discussion, Formal analysis; **Wen-qing MA:** Experiment design, Literature research, Data analysis, Supervision, Funding acquisition, Writing − Original draft, Writing − Review & editing; **Cai-xia XU:** Supervision, Funding acquisition, Writing − Review & editing.

Declaration of competing interest

The authors declare that they have no known competing financial interests or personal relationships that could have appeared to influence the work reported in this paper.

Acknowledgments

This work was financially supported by the Natural Science Foundation of Shandong Province, China (Nos. ZR2023ME155, ZR2023ME085), the National Natural Science Foundation of China (No. 52201254), the Project of “20 Items of University” of Jinan, China (No. 202228046), and the Taishan Scholar Project of Shandong Province, China (No. tsqn202306226).

Supporting Information

Supporting Information in this paper can be found at: http://tnmsc.csu.edu.cn/download/17-p3693-2023-0327-Supporting_Information.pdf.

References

[1] BLANC L E, KUNDU D, NAZAR L F. Scientific challenges for the implementation of Zn-ion batteries [J]. Joule, 2020, 4: 771−799.

[2] LIU An-ni, WU Feng, ZHANG Yi-xin, ZHOU Jia-hui, ZHOU Yao-zong, XIE Man. Insight on cathodes chemistry for aqueous zinc-ion batteries: From reaction mechanisms, structural engineering, and modification strategies [J]. Small, 2022, 18: 2201011.

[3] GUO Cong, YI Shan-jun, SI Rui, XI Bao-juan, AN Xu-guang, LIU Jie, LI Jing-fa, XIONG Sheng-lin. Advances on defect engineering of vanadium-based compounds for high-energy aqueous zinc-ion batteries [J]. Advanced Energy Materials, 2022, 12: 2202039.

[4] LIU Cun-xin, XIE Xue-song, LU Bing-an, ZHOU Jiang, LIANG Shu-quan. Electrolyte strategies toward better zinc-ion batteries [J]. ACS Energy Letters, 2021, 6: 1015−1033.

[5] ZHANG Dong-dong, CAO Jin, ZHANG Xin-yu, INSIN N, WANG Shan-min, HAN Jian-tao, ZHAO Yu-sheng, QIN Jia-qian, HUANG Yun-hui. Inhibition of manganese dissolution in Mn_2O_3 cathode with controllable Ni^{2+} incorporation for high-performance zinc ion battery [J]. Advanced Functional Materials, 2021, 31: 2009412.

[6] LIU Zhen, HE Han-bing, LUO Ze-xiang, WANG Xiao-feng, ZENG Jing. 3D printing of customized MnO_2 cathode for aqueous zinc-ion batteries [J]. Transactions of Nonferrous Metals Society of China, 2023, 33: 1193−1204.

[7] TIAN Hua-jun, FENG Guang-xia, WANG Qi, LI Zhao, ZHANG Wei, LUCERO M, FENG Zhen-xing, WANG Zi-le, ZHANG Yu-ning, ZHEN Cheng, GU Meng, SHAN Xiao-nan, YANG Yang. Three-dimensional Zn-based alloys for dendrite-free aqueous Zn battery in dual-cation electrolytes [J]. Nature Communications, 2022, 13: 7922.

[8] LI Cui-xia, YUAN Wen-tao, LI Chi, WANG Huan, WANG Liu-bin, LIU Yong-chang, ZHANG Ning. Boosting $Li_3V_2(PO_4)_3$ cathode stability using a concentrated aqueous electrolyte for high-voltage zinc batteries [J]. Chemical Communications, 2021, 57: 4319−4322.

[9] ZHANG Ning, DONG Yang, JIA Ming, BIAN Xu, WANG Yuan-yuan, QIU Man-de, XU Jian-zhong, LIU Yong-chang, JIAO Li-fang, CHENG Fang-yi. Rechargeable aqueous $Zn-V_2O_5$ battery with high energy density and long cycle life [J]. ACS Energy Letters, 2018, 3: 1366−1372.

[10] ZHANG Ning, CHENG Fang-yi, LIU Yong-chang, ZHAO Qing, LEI Kai-xiang, CHEN Cheng-cheng, LIU Xiao-song, CHEN Jun. Cation-deficient spinel $ZnMn_2O_4$ cathode in $Zn(CF_3SO_3)_2$ electrolyte for rechargeable aqueous Zn-ion battery [J]. Journal of the American Chemical Society, 2016, 138: 12894−12901.

[11] ZANG Xiao-bei, LI Ling-tong, SUN Zhi-xin, BOUKHERROUB R, MENG Jia-xin, CAI Kun-peng, SHAO Qing-guo, CAO Ning. A simple physical mixing method for MnO_2/MnO nanocomposites with superior Zn^{2+} storage performance [J]. Transactions of Nonferrous Metals Society of China, 2020, 30: 3347−3355.

[12] TAN Qiu-yang, LI Xue-ting, ZHANG Bao, CHEN Xu, TIAN Ya-wen, WAN Hou-zhao, ZHANG Li-shang, MIAO Ling, WANG Cong, GAN Yi, JIANG Jian-jun, WANG Yi, WANG Hao. Valence engineering via in situ carbon reduction on octahedron sites Mn_3O_4 for ultra-long cycle life aqueous Zn-ion battery [J]. Advanced Energy Materials, 2020, 10: 2001050.

[13] XIONG Ting, YU Zhi-gen, WU Hai-jun, DU Yong-hua, XIE Qi-dong, CHEN Jing-sheng, ZHANG Yong-wei, PENNYCOOK S J, LEE W S V, XUE Jun-min. Defect engineering of oxygen-deficient manganese oxide to achieve high-performing aqueous zinc ion battery [J]. Advanced Energy Materials, 2019, 9: 1803815.

[14] ZHANG Lu, XIAO Chen-yi, LI Jing-jie, YAN Yao-dong, LIU Yong. Facial synthesize of MnO_2 coated carbon sphere for “rocking-chair” capacitive deionization [J]. Journal of Liaocheng University (Natural Science Edition), 2023, 36: 41−47. (In Chinese)

[15] ZHU Chu-yu, FANG Guo-zhao, LIANG Shu-quan, CHEN Zi-xian, WANG Zi-qing, MA Jing-yuan, WANG Han, TANG Bo-ya, ZHENG Xu-sheng, ZHOU Jiang. Electrochemically induced cationic defect in MnO intercalation cathode for aqueous zinc-ion battery [J]. Energy Storage Materials, 2020, 24: 394−401.

[16] XU Shu-jun, FAN Si-wei, MA Wen-qing, FAN Jia-bao, LI Guang-da. Electrochemical reaction behavior of MnS in aqueous zinc ion battery [J]. Inorganic Chemistry Frontiers, 2022, 9: 1481−1489.

[17] WU Yun-zhao, TAO Ye, ZHANG Xian-fu, ZHANG Kai, CHEN Sheng-bin, LIU Yu, DING Yong, CAI Mo-lang, LIU Xue-peng, DAI Song-yuan. Self-assembled α-MnO_2 urchin-like microspheres as a high-performance cathode for aqueous Zn-ion batteries [J]. Science China Materials, 2020, 63: 1196−1204.

[18] PAN Hui-lin, SHAO Yu-yan, YAN Peng-fei, CHENG Ying-wen, HAN K S, NIE Zi-min, WANG Chong-min, YANG Ji-hui, LI Xiao-lin, BHATTACHARYA P, MUELLER K T, LIU Jun. Reversible aqueous zinc/manganese oxide energy storage from conversion reactions [J]. Nature Energy, 2016, 1: 16039.

[19] WANG Wei, LI Hai-bo. Controlled synthesis of ε-MnO_2 nanosheets and its capacitive deionization behaviors [J]. Journal of Liaocheng University (Natural Science Edition), 2023, 36: 82−89. (In Chinese)

[20] LI Lie-wu, WANG Li-ping, ZHANG Ming-yu, HUANG Qi-zhong, HE Ke-jian, WU Fei-xiang. Enhancement of lithium storage capacity and rate performance of Se-modified MnO/Mn_3O_4 hybrid anode material via pseudocapacitive behavior [J]. Transactions of Nonferrous Metals Society of China, 2020, 30: 1904−1915.

[21] XIONG Ting, ZHANG Yao-xin, LEE W S V, XUE Jun-min. Defect engineering in manganese-based oxides for aqueous rechargeable zinc-ion batteries: A review [J]. Advanced Energy Materials, 2020, 10: 2001769.

[22] CHENG Jin, ZHANG Zheng-fu, ZHAO Yi-qun, YU Wen-long, HOU Hong-ying. Effects of additives on performance of zinc electrode [J]. Transactions of

Nonferrous Metals Society of China, 2014, 24: 3551−3555.

[23] FU Yan-qing, WEI Qi-liang, ZHANG Gai-xia, WANG Xiao-min, ZHANG Ji-hai, HU Yong-feng, WANG Dong-niu, ZUIN L, ZHOU Tao, WU Yu-cheng, SUN Shu-hui. High-performance reversible aqueous Zn-ion battery based on porous MnO_x nanorods coated by MOF-derived N-doped carbon [J]. Advanced Energy Materials, 2018, 8: 1801445.

[24] FENG Ting-ting, YANG Jian, DAI Si-yi, WANG Jun-chao, WU Meng-qiang. Microemulsion synthesis of $ZnMn_2O_4$/Mn_3O_4 sub-microrods for Li-ion batteries and their conversion reaction mechanism [J]. Transactions of Nonferrous Metals Society of China, 2021, 31: 265−276.

[25] MA Wen-qing, LU Shan-shan, LEI Xiao-feng, LIU Xi-zheng, DING Yi. Porous Mn_2O_3 cathode for highly durable Li−CO_2 batteries [J]. Journal of Materials Chemistry A, 2018, 6: 20829−20835.

[26] CHEN Xian-hong, RUAN Peng-chao, WU Xian-wen, LIANG Shu-quan, ZHOU Jiang. Crystal structures, reaction mechanisms, and optimization strategies of MnO_2 cathode for aqueous rechargeable zinc batteries [J]. Acta Physico Chimica Sinica, 2022, 38: 2111003.

[27] HAN Ming-ming, YAO Jing-jing, HUANG Ji-wu, TANG Yan, WU Xian-wen, LU Bing-an, ZHOU Jiang. Synergistic chemical and electrochemical strategy for high-performance Zn//MnO_2 batteries [J]. Chinese Chemical Letters, 2023, 34: 107493.

[28] LIU Zhe-xuan, YANG Yong-qiang, LU Bing-an, LIANG Shu-quan, FAN Hong-Jin, ZHOU Jiang. Insights into complexing effects in acetate-based Zn-MnO_2 batteries and performance enhancement by all-round strategies [J]. Energy Storage Materials, 2022, 52: 104−110.

[29] LI Dong, WANG Zi-rui, XIA Yong-mei, GAO Qing-li, REN Man-man, LIU Wei-liang, KONG Fan-gong, WANG Shou-juan, LI Song-hao. Copper-doped manganese tetroxide composites with excellent electrochemical performance for aqueous zinc-ion batteries [J]. Journal of Electroanalytical Chemistry, 2021, 888: 115214.

[30] DAI Lin-na, SUN Qing, CHEN Li-na, GUO Huan-huan, NIE Xiang-kun, CHENG Jun, GUO Jian-guang, LI Jian-wei, LOU Jun, CI Li-jie. Ag doped urchin-like α-MnO_2 toward efficient and bifunctional electrocatalysts for Li−O_2 batteries [J]. Nano Research, 2020, 13: 2356−2364.

[31] HAO Qin, YU Yang, ZHAO Dian-yun, XU Cai-xia. Composited Co_3O_4/Ag with flower-like nanosheets anchored on a porous substrate as a high-performance anode for Li-ion batteries [J]. Journal of Materials Chemistry A, 2015, 3: 15944−15950.

[32] HUANG Peng, WANG Xin-yuan, Hao Qin, Zhou Ji, XU Cai-xia. Preparation of 3D hierarchical molybdenum-polydopamine microflowers as cathode for aqueous Zinc-ion batteries with large voltage range [J]. Journal of Liaocheng University (Natural Science Edition), 2023, 36: 85−92. (In Chinese)

[33] ZHANG Man-shu, WU Wei-xing, LUO Jia-wei, ZHANG Hao-zhe, LIU Jie, LIU Xiao-qing, YANG Yang-yi, Lu Xi-hong. A high-energy-density aqueous zinc-manganese battery with a La−Ca co-doped ε-MnO_2 cathode [J]. Journal of Materials Chemistry A, 2020, 8: 11642−11648.

[34] ZHU Jin-yun, JIAN Tian-zhen, WU Yu-xin, MA Wen-qing, LU Yao, SUN Ling-chao, MENG Fan-hui, WANG Bo, CAI Fei-peng, GAO Jin-hua, LI Guang-da, YANG Li-shan, YAN Xiu-ling, XU Cai-xia. A highly stable aqueous Zn/VS_2 battery based on an intercalation reaction [J]. Applied Surface Science, 2021, 544: 148882.

[35] MA Wen-qing, WANG Ya-hui, YANG Yi-jun, WANG Xi, YUAN Zhi-hao, LIU Xi-zheng, DING Yi. Temperature-dependent Li storage performance in nanoporous Cu−Ge−Al alloy [J]. ACS Applied Materials & Interfaces, 2019, 11: 9073−9082.

[36] XU Cai-xia, HAO Qin, ZHAO Dian-yun. Facile fabrication of a nanoporous Si/Cu composite and its application as a high-performance anode in lithium-ion batteries [J]. Nano Research, 2016, 9: 908−916.

[37] HAO Qin, HOU Jia-gang, YE Jia-jia, YANG Hong-xiao, DU Jia-lei, XU Cai-xia. Hierarchical macroporous Si/Sn composite: Easy preparation and optimized performances towards lithium storage [J]. Electrochimica Acta, 2019, 306: 427−436.

[38] HAO Qin, WANG Jin-ping, XU Cai-xia. Facile preparation of Mn_3O_4 octahedra and their long-term cycle life as an anode material for Li-ion batteries [J]. Journal of Materials Chemistry A, 2014, 2: 87−93.

[39] XU Cai-xia, WANG Rong-yue, ZHANG Yan, DING Yi. A general corrosion route to nanostructured metal oxides [J]. Nanoscale, 2010, 2: 906−909.

[40] JIAN Tian-zhen, MA Wen-qing, XU Cai-xia, LIU Hong, WANG J. Intermetallic-driven highly reversible electrocatalysis in Li−CO_2 battery over nanoporous Ni_3Al/Ni heterostructure [J]. eScience, 2023, 3: 100114.

[41] ZHANG Shao-fei, ZHANG Zhi-jia, ZHANG Xi-yuan, KANG Jian-li. Carbon coated $Ni_xCo_yMn_{1-x-y}O$/Mn_3O_4 with robust deficiencies grown on nanoporous alloy for enhanced Li-ion storage [J]. Electrochimica Acta, 2020, 332: 135468.

[42] SUN Quan-hu, HE Jian-jiang, LI Xiao-dong, LU Tian-tian, SI Wen-yan, ZHAO Fu-hua, WANG Kun, HUANG Chang-shui. In-situ synthesis of graphdiyne on Mn_3O_4 nanoparticles for efficient Zn ions diffusion and storage [J]. Chemical Engineering Journal, 2022, 432: 134402.

[43] HUANG Can, WANG Qiu-fan, TIAN Guo-fu, ZHANG Dao-hong. Oxygen vacancies-enriched Mn_3O_4 enabling high-performance rechargeable aqueous zinc-ion battery [J]. Materials Today Physics, 2021, 21: 100518.

[44] JIAN Tian-zhen, ZHU Jin-yun, MA Wen-qing, YAN Xiu-ling, LI Guang-da, ZHOU Jian-hua. Interconnected two-dimensional MnO_2 nanosheets anchored on three-dimensional porous Cu skeleton as a high-performance cathode for energy storage [J]. Applied Surface Science, 2020, 529: 147152.

[45] PENG Bo, CHEN Yan-xu, WANG Feng, SUN Zhi-hao, ZHAO Li-ping, ZHANG Xiao-lei, WANG Wen-tao, ZHANG Gen-qiang. Unusual site-selective doping in layered cathode strengthens electrostatic cohesion of alkali-metal layer for practicable sodium-ion full cell [J]. Advanced Materials, 2022, 34: 2103210.

[46] XU Jun-wei, WANG Jin-guo, GE Lin-heng, SUN Jun-ru, MA Wen-qing, REN Man-man, CAI Xiao-xia, LIU Wei-liang, YAO Jin-shui. ZIF-8 derived porous carbon to mitigate shuttle effect for high performance aqueous zinc–iodine batteries [J]. Journal of Colloid and Interface Science, 2022, 610: 98−105.

Ag 掺杂和交联双修饰策略提升 Mn_3O_4 的储锌性能

王欣媛[1]，简天真[1]，杨雅婷[1]，马建平[2]，李现红[2]，薛子龙[1]，马文庆[1,2,3]，徐彩霞[1]

1. 济南大学 化学化工学院 山东省生物诊断与治疗技术设备协同创新中心 前沿交叉科学研究院，济南 250022；
2. 山东圣阳电源股份有限公司，曲阜 273100；
3. 山东大学 晶体材料国家重点实验室，济南 250100

摘　要：通过合金化−刻蚀工程制备 Ag 掺杂和纳米多孔 Ag (NPS)交联的 Mn_3O_4 八面体纳米颗粒。所制备的双修饰 Mn_3O_4 (Ag−Mn_3O_4/NPS)由 Ag 掺杂的 Mn_3O_4 八面体和纳米多孔银骨架交联构成。Ag 的晶格掺杂能够有效改善 Mn_3O_4 阴极材料的离子和电子电导率，而 NPS 框架可以改善整个电极的电子/物质传输效率。得益于双修饰策略，Ag−Mn_3O_4/NPS 表现出高的倍率和循环性能，在 1 A/g 的电流密度下循环 1000 次后仍可获得 88.7 mA·h/g 的高可逆容量。此外，一系列非原位实验技术证明了 Ag−Mn_3O_4/NPS 的储锌机制：其在首次充电过程中被电化学氧化为多种 MnO_x (如 Mn_2O_3, MnO_2)，后续的电池反应为 H^+和 Zn^{2+}在 MnO_x 中的嵌入/脱出。

关键词：Ag 掺杂 Mn_3O_4；锌离子电池；纳米多孔 Ag；脱合金化

(Edited by Xiang-qun LI)